Journal of Vacuum Science and Technology B

RESEARCH ARTICLE | MARCH 25 2026

Fabrication optimization of suspended stencil mask lithography for multi-terminal Josephson junctions

Justus Teller ; Abdur Rehman Jalil ; Florian Lentz ; Detlev Grützmacher ; Thomas Schäpers

J. Vac. Sci. Technol. B 44, 032801 (2026)
https://doi.org/10.1116/6.0005295

JVST B
Journal of Vacuum Science & Technology B

ARTICLE

pubs.aip.org/avs/jvb

Fabrication optimization of suspended stencil mask lithography for multi-terminal Josephson junctions

Cite as: J. Vac. Sci. Technol. B **44**, 032801 (2026); doi: 10.1116/6.0005295
Submitted: 9 January 2026 · Accepted: 9 March 2026 ·
Published Online: 25 March 2026

View Online Export Citation CrossMark

Justus Teller,[1,2,a)] Abdur Rehman Jalil,[3] Florian Lentz,[4] Detlev Grützmacher,[1,2] and Thomas Schäpers[1,2,b)]

AFFILIATIONS

[1]Peter Grünberg Institut (PGI-9), Forschungszentrum Jülich, Jülich 52425, Germany
[2]JARA-Fundamentals of Future Information Technology, Jülich-Aachen Research Alliance, Forschungszentrum Jülich and RWTH Aachen University, Jülich 52425, Germany
[3]Peter Grünberg Institut (PGI-10), Forschungszentrum Jülich, Jülich 52425, Germany
[4]Helmholtz Nano Facility, Forschungszentrum Jülich, Jülich 52425, Germany

[a)]**Electronic mail:** j.teller@fz-juelich.de
[b)]**Electronic mail:** th.schaepers@fz-juelich.de

ABSTRACT

Stencil mask lithography is an advanced technique for fully *in situ* fabricating Josephson junctions, which is increasingly being used for multiterminal Josephson junctions. This study provides information on the optimal mask design and mask reliability. For this, 270 mask designs were systematically fabricated and investigated under a scanning electron microscope. Reliable statements are made about mask yield, minimal dimensions, and systematic dependencies on the number of superconducting terminals. We find that stencil mask lithography can be used reliably for fabricating multiterminal Josephson junctions, enabling lateral mask dimensions down to 40 nm on average.

I. INTRODUCTION

Stencil mask lithography has a rich history dating back to 1969.[1,2] In contrast to resist patterning, possible functionalities of stencil masks include to keep them at a distance from the substrate, to move them during processing, and to use them multiple times, since they are mechanically stable and self-supporting.[2] Moreover, the technique is scalable and applied across several fields.[3] Recent developments include the fabrication of complex three-dimensional (3D) surfaces and self-aligned superlattices,[4] a plasmonic metasurface of 3D inclined structures,[5] next-generation biochemical sensors,[6] stretchable conductors,[7] and transmon qubits.[8]

In 2019, Schüffelgen *et al.*[9] introduced stencil mask lithography for the fabrication of Josephson junctions with normal-conducting weak link. The advantage of this *in situ* fabrication technique is that all material layers can be deposited by molecular beam epitaxy (MBE) or electron beam evaporation without breaking the ultrahigh vacuum. Consequently, the material interfaces are exceptionally clean, free of residual interface atoms or oxidation. In a superconductor-normal conductor-superconductor (SNS) junction, the Josephson supercurrent flows between two closely spaced superconducting electrodes bridged by the normal-conducting weak-link material. The smaller the separation, the larger the superconducting coupling. Using a stencil mask to deposit the superconducting material, the distance between the superconducting electrodes is defined by the width of the mask. The stencil mask technique can be used to fabricate any kind of SNS weak link Josephson junction, comprising different weak link materials, such as metals, semiconductors, or topological materials. Over the last few years, a broad range of research studies have been published using this fabrication technique, including two-terminal Josephson junctions,[9–15] three-terminal Josephson junctions,[16,17] and whole networks of Josephson junctions.[18]

In general, more complex Josephson junctions, i.e., multiterminal junctions, have attracted increasing attention recently.[19–25] They are defined as a Josephson junction with more than two superconducting contacts that all share the same weak link.[20,23,26] For multiterminal Josephson junctions, one can distinguish between two model descriptions: In the first model, all superconducting weak link channels meet at a central scattering region in the middle[20,23,24,26–28] (central scattering transport model) and, in the second model, each superconducting contact pairwise shares transport channels with a neighboring one in a network.[21,22,29,30] The latter can be described by a resistively and capacitively shunted junction network using Kirchhoff's circuit laws.[22,30] The central scattering model is of great interest because it allows direct coupling of multiple electrodes, thereby enabling novel device functionalities.[28] Furthermore, it is predicted that artificial topological states can be created, e.g., topological Weyl singularities.[20,31] However, achieving the central scattering region model poses particular challenges for the junction geometry, i.e., all electrodes should be as close as possible in the center part of the device. Regarding multiterminal junctions, Reinhardt *et al.*[32] state that the spatial extent of the superconducting coupling in Josephson junctions is determined by the spatial extent of the Andreev bound states. For this spatial extent, the relevant length scales are the coherence length $\xi_0 = \hbar v_F/\pi\Delta^*$, with v_F being the Fermi velocity and Δ^* being the proximitized superconducting gap in the normal conductor, as well as the mean free path l_e in the normal conductor. So the required spatial focus of the central weak link region, for the central scattering transport model, depends on the chosen materials for the multiterminal Josephson junction.

This study systematically investigates the optimal geometric fabrication parameters for stencil masks of two-, three-, and four-terminal Josephson junctions. Figure 1(a) illustrates the layout of a stencil mask for a three-terminal Josephson junction. The suspended Si_3N_4 mask rests on three SiO_2 pillars. The weak-link material of the junction, e.g., a metal, semiconductor, or topological material, is present under the bridge. One way to define the weak-link geometry *in situ* is to employ selective-area growth, as described by Schüffelgen *et al.*[9] When the superconductor layer is deposited at a fixed angle from above, it casts a shadow corresponding to the mask layout [cf. Fig. 1(b)]. This defines the separation of the superconducting electrodes. After the material deposition for the Josephson junctions, the stencil mask is removed by pulling it away from the sample with a commercially available polymer.[33] This enables further processing on the Josephson junctions, e.g., the deposition of gate dielectric and metal. Therefore, a stencil mask of this study must be newly fabricated for every new Josephson junction and is not reused for several devices. The device fabrication is finished by an etching of the superconductor layer to define separated electrodes, which are later contacted [cf. Fig. 1(c)]. As shown in the inset of Fig. 1(b), the closest distance is achieved in the central region of the mask, where the arms of the mask have the smallest width. A Josephson supercurrent is expected to flow here. Mask optimization occurs within a trade-off context: the wider a stencil mask is, the more stable it is. However, the resulting coupling via the weak link of the Josephson junction is becoming smaller. To achieve good superconducting coupling, we therefore focus on fabricating the masks as narrow as possible but stable at the same time. We will also discuss how to ensure that the fabrication process leaves the mask intact. The masks are designed in a way that each contact is closest to every other contact in the center of the weak link, making the central scattering region transport model more likely.

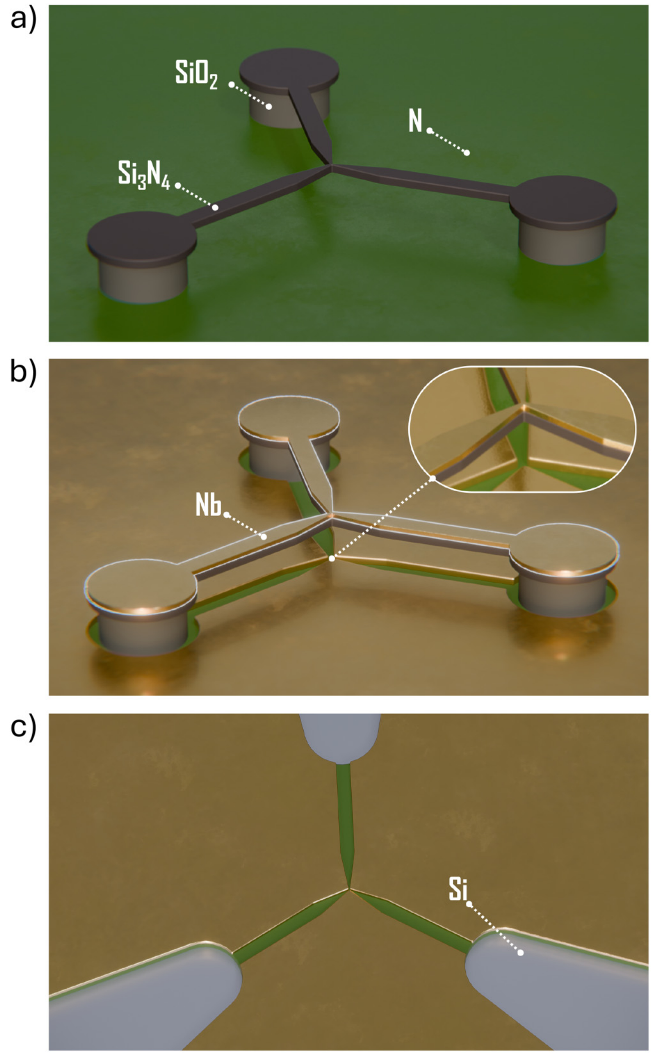

FIG. 1. (a) Visualization of a suspended stencil mask for a three-terminal junction with normal conducting material (N) deposited underneath. The mask itself is made of three pillars (SiO_2) holding up the top Si_3N_4. (b) Deposited Nb on top of the mask. The mask casts a shadow onto the underlying Si substrate. Therefore, the geometry of the mask is directly connected to the resulting device geometry on the substrate. (c) Finished three-terminal junction after mask removal and subsequent etching step to separate the superconducting electrodes, revealing the Si substrate.

For a systematic study on the design limits of stencil masks, we created 270 different mask designs, each one fabricated a total of four times on two different samples. We then investigated by scanning electron microscopy (SEM) which of the masks were broken or intact. For the narrowest intact masks, we looked at how their geometrical dimensions were realized compared to their designed dimensions.

II. MASK FABRICATION

For fabricating the mask, a single 4 in. wafer of Si(111) was covered with a 300 nm-thick SiO_2 layer and a 100 nm-thick Si_3N_4 layer by plasma-enhanced chemical vapor deposition (PECVD) at 350 °C using a mixed-frequency (high-frequency/low-frequency) process.[34,35] This allowed for precise tuning of the intrinsic stress to a low-tensile state of approximately 70 MPa in 100 nm-thick films and 50 MPa in 25 nm-thick films.[36,37] This specific low-tensile range is the key to mask stability. It provides enough tension to prevent the membranes from buckling (which occurs under compressive stress) while remaining well below the fracture threshold that leads to film cracking. Subsequently, the wafer was heated to 1000 °C (5 min) and then diced into $7 \times 7\ \text{mm}^2$ pieces. Two of the pieces were picked randomly close to the wafer center as samples. For patterning the mask, the samples were cleaned with acetone (5 min) and isopropanol (5 min), and then pre-baked at 130 °C (5 min). Then, Medusa photoresist (Medusa 82:AR 600-07, ratio 1:2) was spin coated on the samples (4000 rpm, 30 s) and soft baked at 150 °C (10 min).

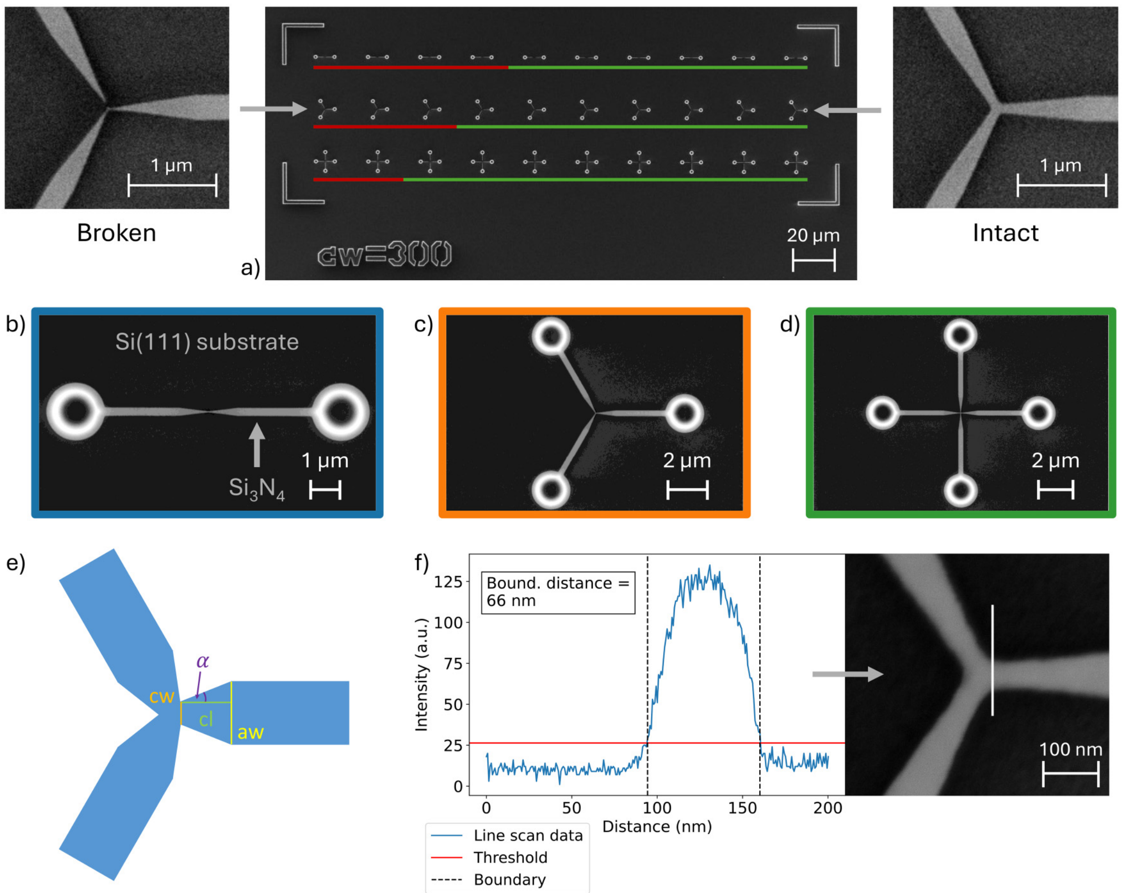

FIG. 2. Fabricated masks and determination of mask dimensions. (a) Scanning electron microscopy image of a fabricated design cell containing three rows for two-, three-, and four-terminal masks, respectively. The arm width was set for each design cell (here $aw = 300$ nm) and the center width was increased from left (10 nm) to right (100 nm) in 10 nm steps. Broken (left) and intact (right) stencil masks were easily identifiable under SEM. The red-marked (on the left) masks were broken and the green-marked (on the right) masks were intact for this particular design cell. (b)–(d) In total, masks for two-, three-, and four- terminal Josephson junctions were investigated. The images correspond to the masks in (a) and their respective frame color equals that of the data, which are presented throughout the study, for the corresponding number of arms. All images show the masks from above. The black region represents the Si(111) substrate and the light gray regions are the Si_3N_4 layer of the mask. The SiO_2 pillars are below the circular ends of the Si_3N_4 layer. (e) Geometry of a three-terminal junction and design parameters used in this study: center width (*cw*), center length (*cl*), and arm width (*aw*). Together, they define the angle of sharpness (α). (f) An exemplary center width measurement of the mask in (c) under SEM using a line scan. The position of the line scan is indicated in the SEM image on the right as a white line. In this particular example, the center width was determined to be $cw = 66$ nm. Information on determining the threshold value (red solid line) is given in the supplementary material.

JVST B
Journal of Vacuum Science & Technology B

Afterward, the pattern was written by electron beam lithography (EBL). The Gaussian beam EBL tool Raith EBPG 5200 with an acceleration voltage of 100 kV was used. The design was split into fine and coarse parts, which were written with beam currents of 500 pA and 150 nA and beam step sizes of 1 and 50 nm, respectively. A multipass scanning mode with four passes was applied for the fine structures while the coarse structures were written in a single pass. The total base dose in both cases amounted to 7096 μC/cm^2 with an additional proximity effect correction with dose factors ranging from 1.0 up to 1.63.

Subsequently, the samples were post exposure baked at 170 °C (10 min) and the resist was developed with AR-300-44 (80 s). The written pattern was then etched into the Si_3N_4 layer by inductively coupled plasma reactive-ion etching (RF power: 25 W, ICP power: 100 W, CHF_3: 55 SCCM, O_2: 5 SCCM, time: 2 min 55 s). Then, the Si_3N_4 layer was under etched by buffered hydrofluoric acid (BOE) (5 min) and 1%-concentrated hydrofluoric acid (3 min). The acid also removed the Medusa photoresist, so the wet-etch step served as a cleaning step as well.

For this study, we created 270 different mask designs using the PHIDL software.[38] All design parameter are given in Fig. 2(e). The designs iteratively change the center width (*cw*) and the arm width (*aw*), whereas the center length (*cl*) stays constant at 1 μm. This results in a change of the angle of sharpness, $\alpha = \arctan[(aw - cw)/2cl]$. A general rule for Josephson junctions is that the smaller the separation of electrodes is, the stronger is the superconducting coupling. Based on that principle, it can be stated that the superconducting coupling is more focused in the center, the larger α is. On a sample, the designs are ordered in the so-called design cells, each having designs with constant arm width [see Fig. 2(a)]. The arm widths range from 100 to 500 nm in 50 nm steps. Within the design cell, there are three rows with designs for two-, three-, and four-terminal masks, respectively. In each row, the center width is increased from 10 to 100 nm in 10 nm steps (from left to right).

III. EXPERIMENTAL RESULTS

In order to evaluate systematically the mask properties, all fabricated masks were inspected by scanning electron microscopy. From every mask, an image was taken on which it is visible whether the mask is broken or intact [see Fig. 2(a)]. Typical failure mechanisms are fractured arms in the mask center, a collapse of the mask center onto the substrate, and collapsing arms due to failure to form the center of the mask (see the supplementary material).

Starting with the first intact mask in each row (from left to right), the geometric parameters *cw* and *aw* were measured using line scans [see Fig. 2(f) and the supplementary material]. These values are used for the discussion in this study.

As mentioned above, the weakest point regarding the mask stability is its narrow middle part. Therefore, it is expedient to look at the probability of mask integrity depending on the center width design parameter *cw*. In general, the center width should be as small as possible to ensure strong Josephson coupling. In Fig. 3, the number of intact masks *N* as a function of the designed center width is given for arm widths *aw* ranging from 100 to 500 nm, i.e.,

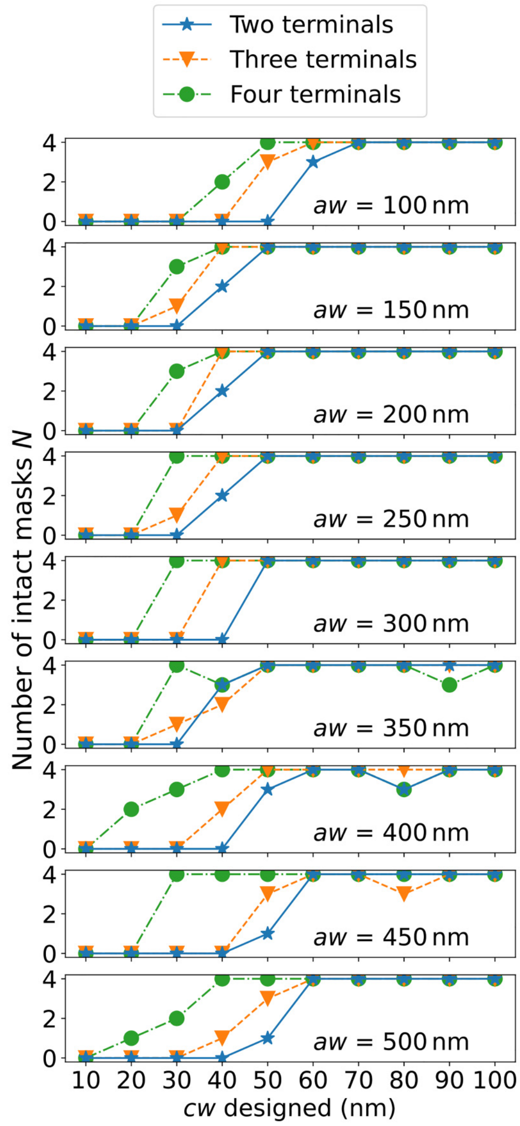

FIG. 3. Number of intact masks *N* depending on the designed center width *cw* and designed arm width *aw* with an accuracy of 25%. The more arms a mask has, the smaller its center width can be designed. Above a certain designed *cw*, the number of intact masks is close to 100%.

for each design cell. A strong dependence between the number of intact masks and center width is evident. One finds that above a certain designed center width, it is possible to fabricate the masks reliably with close to 100 % probability. The more terminals a mask has, the smaller its *cw* can be designed. This is summarized in Fig. 4(a) where, for each arm width *aw*, the optimal (i.e., first intact mask from left to right) *cw* design is indicated. For masks whose *cw* is designed larger than the solid lines, close to 100% yield are expected. Taking the given fixed fabrication parameters for all

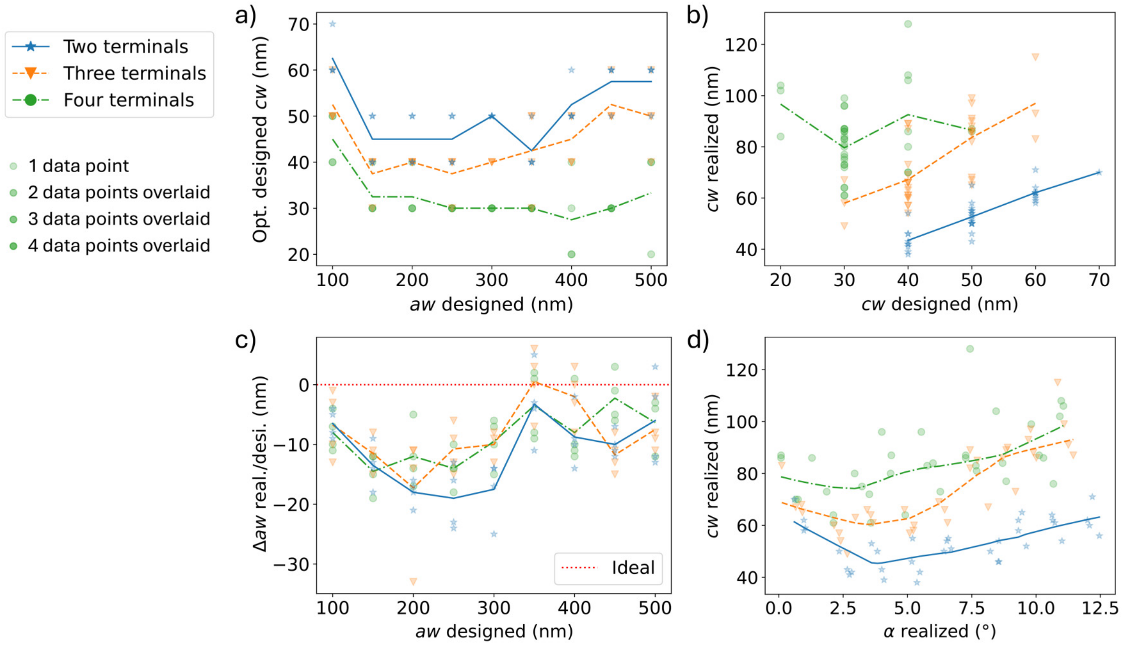

FIG. 4. Geometrical results from the SEM line scans. Each data point is indicated by a marker corresponding to the number of terminals of its mask. The solid lines serve as a guide to the eye [In (a)–(c), the solid lines connect the means of the *y*-values scattering at a certain *x*-value. In (d), the solid lines are determined via locally weighted scatterplot smoothing. See the supplementary material for more details.] and data points are transparent. (a) The optimally designed *cw* depending on the designed *aw*. On average, four-terminal masks can be designed down to 30 nm, three-terminal masks down to 40 nm, and two-terminal masks down to 50 nm. (b) The smallest realized center width *cw* vs designed center width. Two- and three-terminal masks show a linear dependence on *cw* design whereas the realized *cw* of the four-terminal masks scatter around a constant value. (c) The difference between realized and designed arm width. The dashed red (ideal) line indicates the case of matching of the designed and achieved values of *aw*. All values scatter equally around −10 nm. (d) Relation between the realized angle of sharpness α and the realized center width *cw*, assuming an as-designed center length of $cl = 1\,\mu$m.

types of masks into account, the two-terminal masks can be designed down to a *cw* of 50 nm, three-terminal masks down to 40 nm, and four-terminal masks down to 30 nm. However, as discussed below, the actually realized *cw* are larger than the designed *cw* for three- and four-terminal masks.

Since we are interested in the smallest possible dimensions, we will analyze and compare for each type of mask the smallest intact masks we find in the particular rows of the design cells. In the following, the actual geometries of these masks are discussed in detail. In Fig. 4(b), the smallest achieved center widths for the three types of masks are plotted as a function of the designed center widths. We find that contrary to the design limits outlined above, a two-terminal mask can be realized with the smallest center width, whereas the smallest realized *cw* increases the more terminals a mask has. For two-terminal masks, *cw* values as small as 40 nm are obtained. Furthermore, in contrast to the two-terminal masks, the smallest achieved *cw* of the three- and four-terminal masks exceeds the designed values. As indicated by the blue and orange lines in Fig. 4(b), two- and three-terminal masks show quasi-linear behavior between realized and designed *cw*. In contrast, the values of the four-terminal masks scatter around a constant value of 90 nm on average. The reason for both dependencies (contrast between *cw* design limit and realization limit and linear/constant design dependence) is likely the angle between the mask arms, i.e., 180° for two-terminals, 120° for three-terminals, and 90° for four-terminals. Electron beam lithography and wet-etching are both known to have angle dependent fabrication effects: the electron beam lithography is subject to pattern specific linewidth variations by the proximity effect[39,40] and the chemical wet etch rate can be limited by the transport of reactant species to the etched surface as well as the transport of end products away from the surface.[41] These transports are more limited in 90° angles than at straight lines. Although BOE etches the SiO_2 at a significantly higher rate, Si_3N_4 is etched by it as well.

Beside the center width value *cw*, which determines the closest distance between the superconducting electrodes and by that the strength of the superconducting coupling, the angle of sharpness α is of equal importance for multiterminal junctions. It expresses how much the superconducting coupling is restricted to the center part. The larger α is, the more the superconducting electrodes are separated when leaving the junction center. Figure 4(d) shows the relationship between the angle of sharpness, denoted by α, and the minimal width of the center, denoted by *cw*. The minimum center width increases a little bit with increasing α, which can be explained by the proximity effect during electron beam lithography. We routinely realized an angle of sharpness of more than 10°, which is advantageous for obtaining multiterminal junctions operated in the central scattering region transport model.

IV. CONCLUSION

We demonstrated that stencil masks for *in situ* Josephson junction fabrication can be fabricated very reliably with close to 100% probability. Hereby, the masks can be fabricated as small in width as 40 nm. This study should serve as a basis for complex future projects. It gives insights into how to design stencil masks more optimally. A Si(111) substrate was used because it suited our specific needs for growing the topological insulator $(Bi_{0.3}Sb_{0.7})_2Te_3$ on it. Since we use dry etching to release the mask, the stencil mask is independent of the crystal orientation of the substrate. Therefore, we expect similar mechanical stability on Si(100), provided the same PECVD stress tuning is applied. However, this study is limited to the fabrication of the stencil masks themselves; material deposition was neglected. Once a material is deposited on the masks, the additional strain might break the most unstable ones. Therefore, it is advisable to leave some room for failure in future mask designs. The deposition-induced stress depends on the choice of material to be deposited and its thickness. From our experience, working with 15 nm-thick $(Bi_{0.3}Sb_{0.7})_2Te_3$ and 50 nm-thick Nb, adding 30 nm to the design center width of two- and four-terminal masks, and adding 20 nm to three-terminal masks, as a precaution, work reliably. Additionally, there is the option to use an entrenched mask instead of a suspended one (e.g., cf. Ref. 15). Other mask geometries will likely follow the principles outlined in this work.

In future, one could use the PHIDL software[38] in connection with the results of this study to create a library of reliable masks to choose from for projects. This work will enable other researchers to fabricate Josephson junctions with extremely small weak link lengths using the stencil mask lithography technique. In general, stencil masks work reliably for short weak links as well as for multiterminal Josephson junctions.

SUPPLEMENTARY MATERIAL

See the supplementary material for an explanation of the technique used to determine geometrical values from the scanning electron micrographs, a comment on the methods used to show data in Fig. 4, a discussion about mask failure mechanisms as well as out-of-plane bending, and a comparison of the two samples of this study.

ACKNOWLEDGMENTS

We thank Herbert Kertz for technical assistance and Sebastian Droege for the stencil mask visualizations (Fig. 1). All samples have been prepared at the Helmholtz Nano Facility.[42] This work is funded by the Deutsche Forschungsgemeinschaft (DFG, German Research Foundation) under Germany's Excellence Strategy—Cluster of Excellence Matter and Light for Quantum Computing (ML4Q) EXC 2004/1–390534769, by the German Federal Ministry of Education and Research (BMBF) via the Quantum Future project "MajoranaChips" (Grant No. 13N15264), as well as the Bavarian Ministry of Economic Affairs, Regional Development and Energy within Bavaria's High-Tech Agenda Project "Bausteine für das Quantencomputing auf Basis topologischer Materialien mit experimentellen und theoretischen Ansätzen" (Grant No. 07 02/686 58/1/21 1/22 2/23).

AUTHOR DECLARATIONS

Conflict of Interest

The authors have no conflicts to disclose.

Author Contributions

Justus Teller: Conceptualization (lead); Data curation (lead); Formal analysis (lead); Investigation (lead); Methodology (lead); Visualization (lead); Writing – original draft (lead); Writing – review & editing (equal). **Abdur Rehman Jalil:** Conceptualization (equal); Formal analysis (supporting); Writing – original draft (supporting); Writing – review & editing (supporting). **Florian Lentz:** Methodology (equal); Writing – original draft (equal). **Detlev Grützmacher:** Funding acquisition (equal); Project administration (equal); Writing – review & editing (equal). **Thomas Schäpers:** Conceptualization (equal); Funding acquisition (lead); Supervision (lead); Visualization (supporting); Writing – original draft (equal); Writing – review & editing (equal).

DATA AVAILABILITY

The data that support the findings of this article are openly available in Jülich DATA, Ref. 43.

REFERENCES

[1] E. C. Alix, J. Chem. Educ. **46**, 863 (1969).
[2] O. Vazquez-Mena, L. Gross, S. Xie, L. G. Villanueva, and J. Brugger, Microelectron. Eng. **132**, 236 (2015).
[3] K. Du, J. Ding, Y. Liu, I. Wathuthanthri, and C.-H. Choi, Micromachines **8**, 131 (2017).
[4] S. Zeng, T. Tian, J. Oh, Z.-H. Lin, and C.-J. Shih, Nat. Commun. **16**, 3436 (2025).
[5] T.-I. Jeong, S. Kim, S. Kim, M. Shin, A. Gliserin, T. Y. Kang, K. Kim, and S. Kim, Nanophotonics **13**, 1169 (2024).
[6] B. Ali, S. N. Özkan, U. Kerimzade, M. Nasr Esfahani, S. Akinci, Y. Leblebici, E. Öztürk, and B. E. Alaca, ACS Appl. Nano Mater. **7**, 10634 (2024).
[7] Y.-C. Sun, G. Boero, and J. Brugger, ACS Appl. Electron. Mater. **3**, 5423 (2021).
[8] I. Tsioutsios, K. Serniak, S. Diamond, V. V. Sivak, Z. Wang, S. Shankar, L. Frunzio, R. J. Schoelkopf, and M. H. Devoret, AIP Adv. **10**, 065120 (2020).
[9] P. Schüffelgen *et al.*, Nat. Nanotechnol. **14**, 825 (2019).
[10] T. W. Schmitt *et al.*, Nano Lett. **22**, 2595 (2022).
[11] T. W. Schmitt *et al.*, Supercond. Sci. Technol. **36**, 024002 (2023).
[12] D. Rosenbach, A. R. Jalil, T. W. Schmitt, B. Bennemann, G. Mussler, P. Schüffelgen, D. Grützmacher, and T. Schäpers, arXiv:2301.03968 [cond-mat] (2023).
[13] E. Zimmermann *et al.*, Supercond. Sci. Technol. **37**, 085028 (2024).
[14] R. Hanna *et al.*, arXiv:2507.17005 [quant-ph] (2025).
[15] A. R. Jalil *et al.*, Adv. Quantum. Technol. **8**, 2400343 (2025).
[16] J. Kölzer, A. R. Jalil, D. Rosenbach, L. Arndt, G. Mussler, P. Schüffelgen, D. Grützmacher, H. Lüth, and T. Schäpers, Nanomaterials **13**, 293 (2023).
[17] G. Behner, A. R. Jalil, A. Rupp, H. Lüth, D. Grützmacher, and T. Schäpers, ACS Nano **19**, 3878 (2025).
[18] J. Teller, C. Schäfer, K. Moors, B. Bennemann, M. Lyatti, F. Lentz, D. Grützmacher, R.-P. Riwar, and T. Schäpers, Phys. Rev. Lett. **135**, 156002 (2025).

[19]A. H. Pfeffer, J. E. Duvauchelle, H. Courtois, R. Mélin, D. Feinberg, and F. Lefloch, Phys. Rev. B **90**, 075401 (2014).
[20]R.-P. Riwar, M. Houzet, J. S. Meyer, and Y. V. Nazarov, Nat. Commun. **7**, 11167 (2016).
[21]A. W. Draelos *et al.*, Nano Lett. **19**, 1039 (2019).
[22]G. V. Graziano, J. S. Lee, M. Pendharkar, C. J. Palmstrøm, and V. S. Pribiag, Phys. Rev. B **101**, 054510 (2020).
[23]N. Pankratova, H. Lee, R. Kuzmin, K. Wickramasinghe, W. Mayer, J. Yuan, M. G. Vavilov, J. Shabani, and V. E. Manucharyan, Phys. Rev. X **10**, 031051 (2020).
[24]M. Coraiola *et al.*, Nat. Commun. **14**, 6784 (2023).
[25]M. Coraiola *et al.*, ACS Nano **18**, 9221 (2024).
[26]S. Duhot, F. Lefloch, and M. Houzet, Phys. Rev. Lett. **102**, 086804 (2009).
[27]G. V. Graziano, M. Gupta, M. Pendharkar, J. T. Dong, C. P. Dempsey, C. Palmstrøm, and V. S. Pribiag, Nat. Commun. **13**, 5933 (2022).
[28]F. Matute-Cañadas, L. Tosi, and A. L. Yeyati, PRX Quantum **5**, 020340 (2024).
[29]E. G. Arnault *et al.*, Nano Lett. **21**, 9668 (2021).
[30]E. G. Arnault, S. Idris, A. McConnell, L. Zhao, T. F. Larson, K. Watanabe, T. Taniguchi, G. Finkelstein, and F. Amet, Nano Lett. **22**, 7073 (2022).
[31]L. Peralta Gavensky, G. Usaj, and C. A. Balseiro, Europhys. Lett. **141**, 36001 (2023).
[32]S. Reinhardt *et al.*, Phys. Rev. B **112**, 224503 (2025).
[33]See, e.g., First Contact™ cleaning polymer for precision optics.
[34]L. Martinu and D. Poitras, J. Vac. Sci. Technol. A **18**, 2619 (2000).
[35]K. Mackenzie, D. Johnson, M. DeVre, R. Westerman, and B. Reelfs, Meet. Abstr. **MA2005-01**, 406 (2006).
[36]G. Janssen, M. Abdalla, F. Van Keulen, B. Pujada, and B. Van Venrooy, Thin Solid Films **517**, 1858 (2009).
[37]A. R. Jalil, "Engineering topological superlattices and their epitaxial integration in selectively grown hybrid nanostructures via MBE," Ph.D. dissertation (RWTH Aachen University, Aachen, 2022).
[38]A. N. McCaughan, A. N. Tait, S. M. Buckley, D. M. Oh, J. T. Chiles, J. M. Shainline, and S. W. Nam, J. Vac. Sci. Technol. B **39**, 062601 (2021).
[39]L. Ren and B. Chen, in *Proceedings of 7th International Conference on Solid-State and Integrated Circuits Technology*, Beijing, China, 2004 (IEEE, New York City, 2004), Vol. 1, pp. 579–582.
[40]Z. J. Zhou, in *Handbook of Microscopy for Nanotechnology*, edited by N. Yao and Z. L. Wang (Kluwer Academic, Boston, MA, 2005), pp. 287–321.
[41]A. Sarangan, *Nanofabrication: Principles to Laboratory Practice*, Optical Sciences and Applications of Light (CRC Press, Taylor & Francis Group, Boca Raton, 2017).
[42]W. Albrecht, J. Moers, and B. Hermanns, J. Large-Scale Res. Facil. **3**, A112 (2017).
[43]J. Teller, A. R. Jalil, F. Lentz, D. Grützmacher, and T. Schäpers (2025b), "Data for: Fabrication optimization of suspended stencil mask lithography for multi-terminal Josephson junctions," V2, JülichDATA. https://doi.org/10.26165/JUELICH-DATA/7WRRRH.